Dirac's equation and its implications for density functional theory based calculations of materials containing heavy elements

Daniel A. Rehn, John M. Wills, Torey E. Battelle, and Ann E. Mattsson

Phys. Rev. B **101**, 085114 — Published 11 February 2020

DOI: 10.1103/PhysRevB.101.085114

The Dirac equation and its implications for density functional theory-based calculations of materials containing heavy elements

Daniel A. Rehn,[1,2] John M. Wills,[2] Torey E. Battelle,[3] and Ann E. Mattsson[1]

[1] *Computational Physics Division, Los Alamos National Laboratory, Los Alamos, NM 87545, USA*
[2] *Theoretical Division, Los Alamos National Laboratory, Los Alamos, NM 87545, USA*
[3] *Department of Physics, Colorado School of Mines, Golden, CO 80401, USA*

Electronic structure calculations based on density functional theory (DFT) give quantitatively accurate predictions of properties of most materials containing light elements. For heavy materials, and in particular for f-electron systems, DFT-based methods can fail both qualitatively and quantitatively for two distinct reasons: their failure to describe confinement effects arising from localized f-electron behavior and their incomplete or approximate treatment of relativity. In addition, different methods for incorporating relativistic effects, which give identical results in most light materials, can give different predictions in heavy elements. In order to develop a quantitative capability for calculating the properties of these materials, it is essential to separate the predictions of the underlying equations from the uncertainty introduced in approximations used in computation. Working toward that goal, we have developed a code, called `dirac-fp`, which is based directly on solving the Dirac-Kohn-Sham equations and uses the full potential linear muffin tin orbital (FP-LMTO) approach to electronic structure. In order to assess the performance of `dirac-fp`, we perform calculations on three different FCC materials using different approximate treatments of relativity: the scalar relativistic (SR) approach commonly used in most solid-state DFT codes, the scalar relativistic plus spin-orbit coupling corrections (SR+SO) approach which includes spin-orbit coupling self-consistently using the SR states inside the muffin tins, and the Dirac-Kohn-Sham (Dirac) approach implemented in `dirac-fp`. Performing calculations on thorium, in which relativistic effects should be strong, aluminum, in which relativistic effects should be negligible, and gold, in which relativistic effects play an intermediate role, we find that the Dirac approach is able to provide theoretically consistent results in the electronic structure and ground state properties across all three materials.

I. INTRODUCTION

Density functional theory[1] (DFT) provides a theoretical foundation for the accurate calculation of ground-state properties of materials. In particular, the Kohn-Sham methodology,[2] combined with the development of increasingly sophisticated exchange-correlation functionals,[3,4] has enabled quantitative prediction of ground-state properties for many materials. These developments have made DFT an essential and useful tool for a wide variety of applications, including the development of quantitative equations of state for many materials that allow for the study of material response under external stimuli.

While DFT methods based on the Schrödinger equation often work well for materials containing light elements, the same is not always true for materials containing heavy elements. Two separate issues exist. One issue is that for many heavy elements, such as those containing f-electrons, confinement physics can play an essential role. These confinement effects are not captured by standard exchange-correlation functionals. This is not exclusive to f-electron systems, as confinement effects are also present, for example, in the late $3d$ transition metals. The second issue is that relativistic effects, which become increasingly relevant in heavy elements, are not fully captured by methods based on the Schrödinger equation.

The failure of standard methods in describing confinement effects has far-reaching consequences for f-electron systems. Commonly used exchange-correlation functionals are unable to give quantitative predictions for most lanthanides and/or actinides, and often fail even qualitatively. For example, local density approximations (LDAs) and generalized gradient approximations (GGAs) are unable to predict the transition from itinerant to localized electron behavior seen in the α-γ transition in cerium.[5–9] Additionally, GGAs used to study the α, β, γ, δ, δ', and ϵ phases of plutonium generally require some form of orbital correction to the energy to properly describe the relative phase energies and volumes.[10–12] Furthermore, while these functionals give reasonable predictions for the light actinides thorium to neptunium and the ground-states of plutonium and cerium,[13] they do not describe localized electron behavior in the lanthanides past cerium, nor in the actinides past plutonium.[14] Fundamentally, new functionals that take into account confinement physics are needed. Recently, approachces based on the sub-system functional scheme have been proposed as a means to incorporate confinement physics into functionals,[15,16] but as of yet no functional has been fully created and tested.

While better functionals are needed to describe confinement physics, this will not address the more fundamental issue of properly incorporating relativistic effects, which can be relevant for any material containing heavy elements, regardless of whether confinement physics plays a role. Fundamentally, this issue must be addressed with a formulation of DFT based on the Dirac equation. The relativistic formulation of density functional theory (RDFT) based on the Dirac equa-

tion has been formulated theoretically,[17–24] and various levels of approximation to the fully relativistic equations have been introduced in different codes. Examples include a Dirac-Kohn-Sham implementation in the full-potential local-orbital minimum-basis (FPLO) scheme,[25,26] a Dirac-Kohn-Sham implementation using Gaussian-type orbitals for solids,[27] and a four-component relativistic density functional implementation in the Beijing Density Functional (BDF) code.[28,29] Additionally, relativistic effects at the level of the Dirac equation have been studied in the context of quantum chemical methods,[30–32] including the DIRAC code,[33] among others.[34–41]

The difficulty of a complete Dirac-based implementation is due in part to the fact that the exchange-correlation functional has a dependence on both the charge and current density, rather than just the spin-resolved charge density, and therefore new computational schemes and current-density functionals are needed. In conventional DFT codes, relativity is instead incorporated at the scalar relativistic (SR) level, potentially with an added spin-orbit coupling correction (SR+SO), both of which can use exchange-correlation functionals of the spin density. In principle, a proper RDFT approach would involve exchange-correlation functionals of the four-component current density, and it is possible that such current-density functionals would also need to address the issue of confinement effects to provide an accurate methodology for computing ground-state properties of materials containing f-electrons.

Most of the development of electronic structure methods for the lanthanides and actinides has focused on combining DFT with phenomenological models, such as the Hubbard model,[42] to describe electron localization. Within this category are the LDA+U method[43,44] and DFT combined with dynamical mean field theory (DFT+DMFT).[45–47] Such calculations combine two very different methodologies without a clear separation between them and also require parameterization, requiring users to both determine a criteria for choosing the parameter and then testing the results using different values of the parameter. Other approaches include partial summation of electron self-energy diagrams, as in the GW approximation,[48] and the development of Hartree-Fock+RPA methods for exchange and correlation.[49] While these approaches can offer advantages over standard exchange-correlation functionals, their implementation and use are typically done using the SR or SR+SO methods, and not the full Dirac approach. Establishing the Dirac methodology is therefore a first step towards the combined use of the Dirac equation with methods that go beyond the typical LDA and GGA levels of approximation.

In order to rigorously investigate the importance of relativistic effects in materials containing heavy elements, we have developed a code based on the full potential linear muffin tin orbital (FP-LMTO) approach.[50–53] Our code, referred to as `dirac-fp` (short for Dirac-FP-LMTO), is based on the RSPt code,[51,52] but solves the Dirac-Kohn-Sham equations throughout the entire computational cell.

The RSPt and `dirac-fp` codes are frequently used for the study of solids containing heavy elements under compression. In such applications, the Dirac equation becomes increasingly important for several reasons. First, in high compression the core states of materials may start to interact. When this occurs, it is critical to use wavefunctions that exhibit the correct energy level splittings and the correct radial and angular behavior both near the nuclear centers and away from the nuclear centers so that hybridization of Dirac states can be properly incorporated. In the commonly used SR method, SR semicore states do not always exhibit the correct energy level splittings due to the neglect of spin-orbit coupling, as shown for thorium and gold in Sec. III. This may not present serious issues near equilibrium where those states are well-localized and do not interact with each other, but should be expected to lead to errors when studying materials under high compression.

Second, in order to study high compression of heavy materials, it is critical to properly incorporate spin-orbit coupling to account for energy level splittings that influence hybridization behavior. In solid-state physics codes, spin-orbit coupling is most often incorporated using the SR states, referred to as SR+SO. Although this offers advantages, the SR+SO treatment does not by itself lead to the correct $r \to 0$ behavior of certain states, such as the $6p_{1/2}$ states that are very important for studying actinide materials. This point has been studied previously in the context of the `WIEN97` code, where $6p_{1/2}$ states solved using the Dirac equation are added to the SR $6p$ manifold.[54] While this offers advantages over methods that do not correct the $r \to 0$ behavior of the $6p_{1/2}$ states, the other states are still treated using the SR radial equation and therefore exhibit other differences with Dirac states. In addition to this, the angular components of all states, including the corrected $6p_{1/2}$ states, are treated using the SR angular functions, which are different from the Dirac angular functions (see Eqs. 18–19 and refs. 50 and 55 for details). The benefit of the Dirac approach is that all states exhibit the correct Dirac radial behavior, as well as the correct Dirac angular functions, making it possible to correctly incorporate spin-orbit coupling everywhere without the need for additional corrective schemes.

Additional issues arise when treating the spin-orbit interaction differently in different parts of the unit cell. Among all-electron solid-state codes utilizing muffin tin based approaches, including RSPt and `dirac-fp`, it is most common to treat spin-orbit coupling only inside muffin tin spheres using a spherical potential, while not incorporating spin-orbit coupling outside of the muffin tins.[56–59] This treatment is of course an approximation, often justified by the physical argument that spin-orbit coupling is strongest near the nuclear centers contained within the muffin tins, where a spherical potential is sufficient for describing the interactions. In principle, it could

be possible to incorporate spin-orbit corrections outside the muffin tins, for example as done in the Amsterdam Density Functional (ADF)[60] and `FHI-AIMS` codes.[61,62] Nevertheless, it is not obvious how to do this in muffin tin-based codes and the contribution of the spin-orbit term outside the muffin tins is typically neglected.

The neglect of the spin-orbit term in the interstitial is problematic for the FP-LMTO method when determining how to choose the muffin tin radii. One option is to use the fixed-volume-fraction (FF) method, described in detail in Sec. II B. In the FF method, the muffin tin radii are changed as the unit-cell volume changes, leading to a different volume used to treat the spin-orbit term at different unit-cell volumes. This can be compared to fixed radius (FR) methods commonly used in FP-LAPW codes, where the radii are kept fixed as the unit-cell volume is changed. In the FR case, the spin-orbit integration volume therefore does not change as the unit-cell volume is changed. In this study, we present results for both the FF and FR treatments of the SR+SO method (the SR and Dirac cases are not effected by the choice of FF or FR, so long as a full basis is used, as shown in Sec. III A).

Although we present results for both FF and FR for SR+SO, it is critical to point out that we need to be able to use the FF method to study the compression of solids within the FP-LMTO method. There are two reasons for this. First, the most accurate basis in FP-LMTO lies inside the muffin tins, where solutions are atomic-like orbitals, so that it is preferred to use these orbitals throughout as much of the unit cell volume as possible. Although the basis in the interstitial can be quite accurate, sometimes more work is required to ensure its accuracy and it is not always straight-forward how to choose "tail energies" used to form the basis in the interstitial.[52,53] Second, when studying compression, spin-orbit interactions become increasingly important at smaller unit cell volumes. In these cases, using the FR method forces us to throw away large amounts of the spin-orbit interaction because the FR radius must fit within the smallest unit-cell volume studied, thereby placing an upper-bound on the amount of spin-orbit coupling that can be included in calculations. In contrast, the FF method incorporates as much spin-orbit interaction as possible at each unit cell volume, but this also has consequences for the total energy, which contains a changing amount of SO coupling at each volume. Although both of these issues are important, it is not possible to address both issues simulaneously using muffin tin approaches that neglect spin-orbit effects in the interstitial region. Nevertheless, both of these issues are addressed in the Dirac method, where spin-orbit coupling is included in both the muffin tins and the interstitial, and where the full potential, not just a spherically symmetric potential, is used to incorporate spin-orbit contributions using the Dirac radial and angular functions in the construction of matrix elements of the Hamiltonian.

Details on the formulation of the Dirac approach we take and the approximations made therein, as well as how this compares to the SR and SR+SO formulations, are described in Sec. II. Importantly, the SR and SR+SO methods also solve the Dirac equation for the core states, but use the SR or SR+SO approximations for the so-called valence states, as detailed in the following sections. In Sec. III we explore the application of the SR, SR+SO, and Dirac methods to three FCC systems: thorium, where relativistic effects should be strong; aluminum, where relativistic effects should be small or negligible; and gold, where relativistic effects should play an intermediate role. Although relativity is accounted for in `dirac-fp` directly through the use of the Dirac equation, we do not address the issue of the role of confinement physics in the exchange-correlation functional, since as of yet no such functional exists. We therefore explore the use of the Perdew-Wang LDA[63] (PW), the GGA of Perdew, Burke, and Ernzerhof[64] (PBE), and the subsystem functional of Armiento and Mattsson[65](AM05). Although none of these functionals address the issue of confinement physics, they provide a common ground for evaluating the results of the Dirac approach against the SR and SR+SO approaches.

II. THEORETICAL BACKGROUND

A. Relativistic Density Functional Theory

1. *Dirac-Kohn-Sham Equations*

A proper treatment of relativity in DFT calculations must start from the Dirac equation. The formal foundations of such a treatment have been laid out in RDFT.[17–19] There are many summaries of RDFT[20–24] and we take as a starting point the primary result: a set of single-particle Dirac-like equations known as the Dirac-Kohn-Sham equations,

$$\left(c\boldsymbol{\alpha}\cdot\left(\mathbf{p}-\frac{e\mathbf{A}_{\text{eff}}}{c}\right)+\mathbb{1}v_{\text{eff}}(\mathbf{r})+\beta mc^2\right)\psi_n(\mathbf{r})=\varepsilon_n\psi_n(\mathbf{r}). \tag{1}$$

Here,

$$v_{\text{eff}}(\mathbf{r})=-e\left(A^0_{\text{ext}}(\mathbf{r})+\int \mathrm{d}^3r'\frac{J^0(\mathbf{r}')}{|\mathbf{r}-\mathbf{r}'|}+\frac{\delta E_{\text{xc}}[J^\mu]}{\delta J^0(\mathbf{r})}\right) \tag{2}$$

and

$$e\mathbf{A}_{\text{eff}}(\mathbf{r})=-e\left(\mathbf{A}_{\text{ext}}(\mathbf{r})+\int \mathrm{d}^3r'\frac{\boldsymbol{J}(\mathbf{r}')}{|\mathbf{r}-\mathbf{r}'|}+\frac{\delta E_{\text{xc}}[J^\mu]}{\delta \boldsymbol{J}(\mathbf{r})}\right) \tag{3}$$

for all negative and positive energy orbitals. The matrices in Eq. 1 are defined as

$$\alpha_k=\begin{pmatrix}0 & \sigma_k\\ \sigma_k & 0\end{pmatrix},\ \beta=\begin{pmatrix}I & 0\\ 0 & -I\end{pmatrix},\ I=\begin{pmatrix}1 & 0\\ 0 & 1\end{pmatrix},\ \mathbb{1}=\begin{pmatrix}I & 0\\ 0 & I\end{pmatrix}, \tag{4}$$

where σ_k are the Pauli matrices.[55] The Dirac 4-component spinors ψ_n can be represented as

$$\psi_n = \begin{pmatrix} \psi_{1,n} \\ \psi_{2,n} \\ \psi_{3,n} \\ \psi_{4,n} \end{pmatrix} = \begin{pmatrix} \psi_{A,n} \\ \psi_{B,n} \end{pmatrix}. \tag{5}$$

Throughout, we define e to be a negative value, following the notation in refs. 20 and 55,

$$e = -|e|. \tag{6}$$

The conserved current $J^\mu = (J^0, \boldsymbol{J})$ is analogous to the density in non-relativistic DFT and is thus the conserved current of the real system that can be calculated from the spinor solutions to the relativistic Kohn-Sham equations,

$$J^\mu = (J^0, \boldsymbol{J}) = -e \sum_n (\psi_n^\dagger \psi_n, \psi_n^\dagger \boldsymbol{\alpha} \psi_n). \tag{7}$$

The energy computed includes the rest mass energy, so that the energy available for bonding and kinetic energy is $\varepsilon_n - mc^2$.

The vacuum expectation value of the current operator is non-zero. Pairs of electron-positrons can be spontaneously created in vacuum, often referred to as the vacuum polarization. If the vacuum polarization is neglected the current becomes

$$J^\mu = -e \sum_{-mc^2 < \varepsilon_n < \varepsilon_F} (\psi_n^\dagger \psi_n, \psi_n^\dagger \boldsymbol{\alpha} \psi_n), \tag{8}$$

where ε_F is the Fermi energy.

2. *Transition from current functionals to density functionals*

In the non-relativistic formulation of DFT, the currents $\boldsymbol{J}$ that couple to the effective vector potential $\mathbf{A}_{\text{eff}}$ are not used. In order to use the density functionals developed for non-relativistic DFT, we can use the spin density,

$$\mathbf{S} = - \sum_{mc^2 < \varepsilon_n < \varepsilon_F} \psi_n^\dagger \beta \boldsymbol{\Sigma} \psi_n, \tag{9}$$

where

$$\Sigma_k = \begin{pmatrix} \sigma_k & 0 \\ 0 & \sigma_k \end{pmatrix}. \tag{10}$$

For time-independent problems, it is possible to use the Gordon decomposition[66] to write the current density as

$$\boldsymbol{J} = \mathbf{I} + \mu_B \nabla \times \mathbf{S}, \tag{11}$$

where

$$\mathbf{I} = \frac{e}{2mc} \sum_{mc^2 < \varepsilon_n < \varepsilon_F} \left(\psi_n^\dagger \beta \left[\left(\mathbf{p} - \frac{e\mathbf{A}_{\text{eff}}}{c} \right) \psi_n \right] + \text{c.c.} \right). \tag{12}$$

One approximation is to neglect the orbital current $\mathbf{I}$ and use only the spin-density current. In this case, the $e\boldsymbol{\alpha} \cdot \mathbf{A}_{\text{eff}}$ term of Eq. 1 can be simplified, so that the Dirac-Kohn-Sham equations become

$$\left(c\boldsymbol{\alpha} \cdot \mathbf{p} + \mu_B \beta \boldsymbol{\Sigma} \cdot \mathbf{B}_{\text{eff}} + \mathbb{1} v_{\text{eff}}(\mathbf{r}) + \beta mc^2 \right) \psi_n(\mathbf{r}) = \varepsilon_n \psi_n(\mathbf{r}) \tag{13}$$

where $\mathbf{B} = \nabla \times \mathbf{A}$ and μ_B is the Bohr magneton. The term involving $\mathbf{B}_{\text{eff}}$ is

$$\mu_B \mathbf{B}_{\text{eff}}(\mathbf{r}) = \left(\mu_B \mathbf{B}_{\text{ext}}(\mathbf{r}) + \int \mathrm{d}^3 r' \frac{\mathbf{M}(\mathbf{r}')}{|\mathbf{r} - \mathbf{r}'|} + \frac{\delta E_{\text{xc}}[J^0, \mathbf{M}]}{\delta \mathbf{M}(\mathbf{r})} \right), \tag{14}$$

where $\mathbf{M} = \mu_B \mathbf{S}$.

The SR, SR+SO, and Dirac treatments can readily be described in the radial equations of the Hamiltonian. To see this, we first note that within the FP-LMTO method, we expand the effective potential inside the muffin tins as

$$v_{\text{eff}}(\mathbf{r}) = \sum_l v_l(r) \mathcal{C}_l(\theta, \varphi), \tag{15}$$

where the function $\mathcal{C}_l(\theta, \phi)$ is a spherical harmonic with a conveniently chosen multiplicative factor (see refs. 50–53 for details). The expression for the full potential in the interstitial region is also described in refs. 50–53. For non-magnetic materials, such as those studied in Sec. III, it is sufficient to set $\mathbf{B}_{\text{eff}} = 0$. Doing this, Eq. 13 can be separated into equations for the upper and lower components,

$$c\boldsymbol{\sigma} \cdot \mathbf{p} \psi_{B,n}(\mathbf{r}) = (\varepsilon_n - v_{\text{eff}}(\mathbf{r}) - mc^2) \psi_{A,n}(\mathbf{r}) \tag{16}$$

$$c\boldsymbol{\sigma} \cdot \mathbf{p} \psi_{A,n}(\mathbf{r}) = (\varepsilon_n - v_{\text{eff}}(\mathbf{r}) + mc^2) \psi_{B,n}(\mathbf{r}). \tag{17}$$

In order to describe atomic states used in the FP-LMTO method, it is useful to transition to a spherical coordinate system, in which the wavefunctions can be written,

$$\psi = \begin{pmatrix} \psi_A \\ \psi_B \end{pmatrix} = \begin{pmatrix} g(r) \mathscr{Y}_{jl_A}^m(\theta, \varphi) \\ if(r) \mathscr{Y}_{jl_B}^m(\theta, \varphi) \end{pmatrix}, \tag{18}$$

where the angular functions $\mathscr{Y}_{jl}^m(\theta, \varphi)$ are defined as (see refs. 55 and 50)

$$\mathscr{Y}_{jl}^{m}(\theta,\varphi)=\begin{cases}+\sqrt{\frac{l+m+\frac{1}{2}}{2l+1}}Y_l^{m-1/2}(\theta,\varphi)\begin{pmatrix}1\\0\end{pmatrix}+\sqrt{\frac{l-m+\frac{1}{2}}{2l+1}}Y_l^{m+1/2}(\theta,\varphi)\begin{pmatrix}0\\1\end{pmatrix}, & j=l+\frac{1}{2}\\ -\sqrt{\frac{l-m+\frac{1}{2}}{2l+1}}Y_l^{m-1/2}(\theta,\varphi)\begin{pmatrix}1\\0\end{pmatrix}+\sqrt{\frac{l+m+\frac{1}{2}}{2l+1}}Y_l^{m+1/2}(\theta,\varphi)\begin{pmatrix}0\\1\end{pmatrix}, & j=l-\frac{1}{2}.\end{cases} \tag{19}$$

Note that because these angular functions each have two components and are a sum of different spherical harmonics Y_l^m, every component of the four-component Dirac spinors has a different angular dependence, even though the radial functions for the upper and lower components separately are the same. This can be contrasted to the SR and SR+SO approaches, in which only one spherical harmonic is used (see Sec. 2.5 of ref. 50 for details). This is an important distinction between the Dirac and SR or SR+SO approaches that could be important for describing the local bonding environment of materials, particularly for materials under compression.

Using Eqs. 18 and 19 in Eqs. 16–17 and rewriting the operator $\boldsymbol{\sigma}\cdot\mathbf{p}$ in spherical coordinates, we arrive at (see Sec. 2.4 of ref. 50 for details)

$$-c\frac{\mathrm{d}f_\kappa}{\mathrm{d}r}-\frac{(1-\kappa)c}{r}f_\kappa=(\varepsilon_n-v_{\text{eff}}(\mathbf{r})-mc^2)g_\kappa \tag{20}$$

$$c\frac{\mathrm{d}g_\kappa}{\mathrm{d}r}+\frac{(1+\kappa)c}{r}g_\kappa=(\varepsilon_n-v_{\text{eff}}(\mathbf{r})+mc^2)f_\kappa. \tag{21}$$

It is now useful to neglect the non-spherical contributions to v_{eff} in Eq. 15. This allows us to describe the formation of the basis in the FP-LMTO method, in which only the spherical part $v_0(r)$ of v_{eff} is used, and also distinguish between the SR, SR+SO, and Dirac methods, as outlined below. The non-spherical contributions to $v_{\text{eff}}(\mathbf{r})$ are incorporated when computing matrix elements of the Hamiltonian, as described in ref. 50. Restricting v_{eff} to v_0 leads to

$$-c\frac{\mathrm{d}f_\kappa}{\mathrm{d}r}-\frac{(1-\kappa)c}{r}f_\kappa=(\varepsilon_n-v_0(r)-mc^2)g_\kappa \tag{22}$$

$$c\frac{\mathrm{d}g_\kappa}{\mathrm{d}r}+\frac{(1+\kappa)c}{r}g_\kappa=(\varepsilon_n-v_0(r)+mc^2)f_\kappa. \tag{23}$$

By setting $E=\varepsilon_n-mc^2$, $M=m+(E-v_0(r))/2c^2$, and eliminating f_κ, we arrive at the upper component radial equation

$$-\frac{1}{2M}\left(g_\kappa''+\frac{2}{r}g_\kappa'-\frac{l(l+1)}{r^2}g_\kappa\right)-\left(g_\kappa'+\frac{(1+\kappa)}{r}g_\kappa\right)\frac{\mathrm{d}}{\mathrm{d}r}\frac{1}{2M}+v_0(r)g_\kappa=Eg_\kappa, \tag{24}$$

where $\kappa(\kappa+1)=l(l+1)$ is used for both signs of κ. Note that FP-LMTO methods consist of two steps within each self-consistent iteration. In the first step, the linear MTO basis is formed, in which Eq. 24 is solved using v_0. In the second step, matrix elements are formed using the full potential in Eq. 15. That procedure is more involved and we therefore leave its description in the Dirac and also SR and SR+SO cases to Ch. 4 and 5 of ref. 50.

In the fully relativistic Dirac radial equation, Eq. 24, the spin and orbital momenta are not independent constants of the motion but coupled. The coupling is represented by κ, which is the eigenvalue of the operator $\hat{K}=(\boldsymbol{\sigma}\cdot\boldsymbol{\mathcal{L}}+1)\beta$, where $\boldsymbol{\mathcal{L}}$ is the orbital angular momentum operator that squared gives eigenvalue $l(l+1)$.

If the κ-dependent term is dropped, as suggested by Koelling and Harmon,[67] the spin and orbital momenta are decoupled and only l is needed for the description of the resulting solution,

$$-\frac{1}{2M}\left(g_l''+\frac{2}{r}g_l'-\frac{l(l+1)}{r^2}g_l\right)-g_l'\frac{\mathrm{d}}{\mathrm{d}r}\frac{1}{2M}+v_0(r)g_l=Eg_l. \tag{25}$$

The solution given by Eq. 25 is what is referred to as the SR treatment throughout the remainder of the text. The SR treatment naturally leaves out spin-orbit coupling as compared to the full Dirac implementation. Note, however, that the SR and SR+SO approximations still use the Dirac equation (Eq. 24) to compute the core states, as described in the next section. Only the valence states in SR and SR+SO are treated with the SR basis. This is also the common treatment among linearized augmented plane-wave (LAPW) approaches.[68,69]

The SR+SO method solves the SR radial equations (Eq. 25) to form the linear MTO basis in each self-consistent iteration. After this, the full potential (Eq. 15) is incorporated and matrix elements of the spin-orbit operator

$$v_{\text{so}}=\frac{1}{r}\frac{\partial}{\partial r}\left(\frac{1}{2M}\right)\boldsymbol{\sigma}\cdot\mathcal{L} \tag{26}$$

are taken using the SR basis states. It is important to point out that in this step, only the spherical part of the potential v_0 is used in the matrix elements involving Eq. 26 (v_0 enters through the definition of M, defined above). Furthermore, the spin-orbit matrix elements are only taken within the muffin tin spheres because states in the interstitial region have no clear association with the orbital angular momentum and therefore it is not obvious how to apply the spin-orbit term in that spatial region. This means that the treatment of the spin-orbit

term in the SR+SO method is approximate. Although some codes do apply the SO term throughout the full volume,[60,62] most muffin tin based approaches do not treat the spin-orbit term in the interstitial and use a spherically symmetric potential inside the muffin tins.[56–58]

Note that when the SR+SO Hamiltonian is formed using the SR basis functions, two κ terms must be evaluated for each l: $\kappa = l$ and $\kappa = -l - 1$. This amounts to a splitting for each l state when $l > 0$. By including the SO term in the formation of the Hamiltonian within each self-consistent iteration, the SO effects are included fully self-consistently.

Two points about the SR+SO method are worth mentioning. First, although all of the terms in the Dirac equation are present in the SR+SO method, the g_κ values that are plugged in come from the solution of the SR equation, thereby incorporating a different radial behavior in the Hamiltonian than when using the Dirac basis states. Second, the angular functions defined in Eq. 19 are not used in the SR and SR+SO methods. Instead, the same Y_l^m angular functions that describe solutions to the Schrödinger equation are used. As mentioned previously, this could be an important distinction in some cases, though we do not explore this further here.

The SR basis is limited in its ability to describe the SO term,[54,70] so that the SR+SO treatment should not always be expected to give the same results as the full Dirac treatment. This is part of the motivation for the comparisons drawn in this work.

We also point out that in the non-relativistic limit, $M \to m$. In this case, both Eqs. 24 and 25 reduce to

$$-\frac{1}{2m}\left(g_l'' + \frac{2}{r}g_l' - \frac{l(l+1)}{r^2}g_l\right) + v_0(r)g_l = \varepsilon_n g_l, \quad (27)$$

which is the radial Schrödinger equation (SE).

Note that the above mathematical formulation does not provide all of the implementation details of the FP-LMTO method. In the next section, we provide an overview of the FP-LMTO method and additional mathematical details on how the full potential is incorporated in the SR, SR+SO, and Dirac approaches. For a more complete description, see ref. 50.

B. Overview of the FP-LMTO Method

Kohn-Sham DFT electronic structure codes used for solids can be generally divided into two distinct categories: all-electron codes and pseudopotential codes. All-electron codes treat every electron in the material including core states, while pseudopotential codes find an approximate potential (called a pseudopotential) that replaces the core states with an averaged or effective potential that the valence electrons experience. Several types of all-electron methods exist, including those with numerical basis sets,[61] linearly augmented plane wave (LAPW methods),[68,69] and the full potential linear muffin tin orbital (FP-LMTO) approach. These different approaches have been compared in terms of their agreement with each other recently[71] and have shown the all-electron approaches to produce very similar results on a variety of materials, while being generally more accurate than codes using plane-waves and pseudopotentials.

The FP-LMTO methodology used in `dirac-fp` and in RSPt involves splitting the computational cell into a number of spheres (called muffin tins) that each surround a given atom. Inside the muffin tins, the solutions are expanded in terms of atomic-like functions, while outside the muffin tin spheres (also called the interstitial region), the solutions take the form of Hankel or Neumann functions.[51,52] At the boundary between the muffin tins and the interstitial region, the wavefunctions are ensured to be continuous and have continuous first derivatives.

In both `dirac-fp` and RSPt, a distinction is made between core states, which do not extend spatially outside the muffin tin spheres, and the 'valence states,' which exist both within muffin tin spheres and in the interstitial region. The valence states do not necessarily correspond to the *valence electrons*, as it is often useful to move some states from the core (sometimes called the semi-core) to the valence in order to capture hybridization effects. Sometimes the valence states are called 'variational states,' since they are used to form the Hamiltonian which is diagonalized at each self-consistent iteration. However, we refrain from using the term 'variational states' here to avoid the implication that the core states do not vary or are not updated at each self-consistent iteration. As described more below, the core states are being updated at each iteration.

The core states in all methods (SR, SR+SO, and Dirac) are treated using the Dirac equation (Eq. 24). Only the valence states are treated differently in the SR, SR+SO, and Dirac methods. This is shown schematically in Fig. 1. In all calculations, we ensure that the core states do not extend spatially outside of the muffin tins, so that no interactions between core states in separate muffin tins is possible.

The valence states in the SR and SR+SO methods are evaluated using Eq. 25 to form the valence basis, while the Dirac method uses Eq. 24 to form the valence basis. A further spatial subdivision of the valence states is also necessary, since these states exist both inside the muffin tins and in the interstitial region. To account for this, the basis is formed assuming a spherically symmetric potential inside the muffin tins and a constant potential in the interstitial. In the SR and SR+SO methods, the SR basis is used in both the valence and interstitial (shown in Fig. 1; details on how the basis in the interstitial is formed are available in ref. 52). However, in the SR+SO method, the SR basis is used to then incorporate the SO term via Eq. 26 when forming matrix elements of the Hamiltonian. Importantly, the SO term is applied only within the muffin tins, where it is possible to associate the angular momentum quantum number l with the state. In

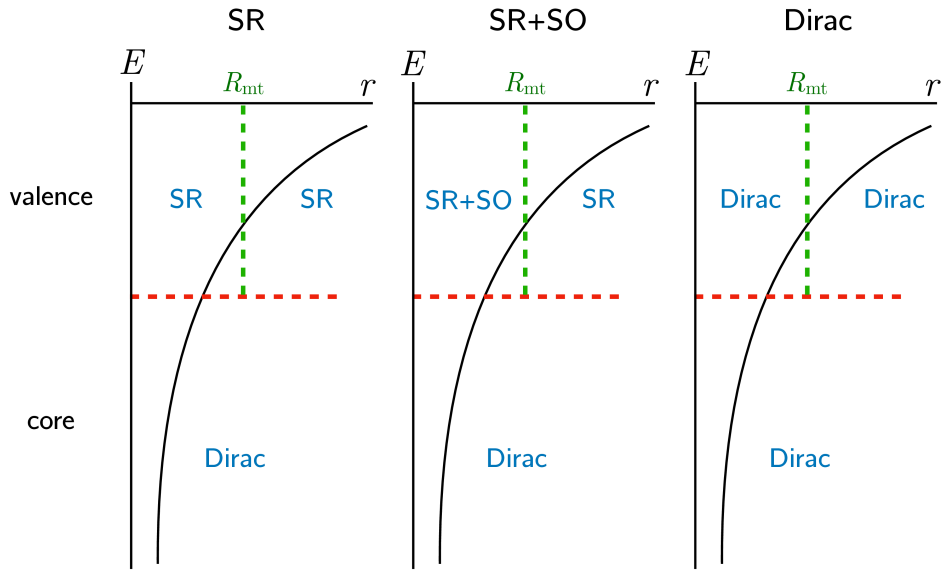

FIG. 1. Schematic of the SR, SR+SO, and Dirac methods within the FP-LMTO methodology. Energy (E) vs. radial distance from the center of a muffin tin sphere (r) is shown, with a representation of full effective potential $v_{\rm eff}(\mathbf{r})$ in the solid black line. All core states are treated using the Dirac equation. The core states and muffin tin radii are chosen so that the core states do not extend spatially outside of the muffin tins and therefore do not interact with other core states. The valence states, which can correspond to states other than the *valence electrons*, are split spatially between a region inside the muffin tins and outside the muffin tins (interstitial region). The SR and SR+SO methods use the SR basis for both spatial regions, while the SO term is only applied within the muffin tins where it is possible to associate the orbital angular momentum with the state. The Dirac method solves the Dirac equation throughout all regions of the cell.

the Dirac method, the Dirac basis states are used in both the muffin tins and interstitial.

It is important to point out that both the valence and core states are updated at each self-consistent iteration in all methods. The core states are modified based on the changes in the eigenvalues E (via ε_n) and the potential $v_0(r)$. However, the core states are not used directly to form the Hamiltonian that is diagonalized in each self-consistent iteration, although the density of the core states contributes to the full potential that effects all states.

The unique property of `dirac-fp` is that all of the wavefunctions (both the core and the valence states) are treated with the Dirac equation. This provides a more consistent treatment of relativistic effects throughout the cell. Aside from this important distinction, `dirac-fp` and RSPt are based on the same methodology and produce the same results when relativistic effects are negligible, as seen in the case of aluminum in Sec. III B.

To fully understand the differences between the SR, SR+SO, and Dirac methods, it is useful to mention a few details regarding the self-consistency cycle in the FP-LMTO method not discussed in Sec. II.

The radial differential equations in Eq. 24,and 25 take the form

$$H_r[v_0]g(r) = Eg(r), \tag{28}$$

where H_r is the radial Hamiltonian. In general, this is a non-linear eigenvalue problem using the potential $v_0(r)$, which is one component of the expansion of the effective potential in Eq. 15. The FP-LMTO method solves this non-linear eigenvalue problem using a self-consistency cycle in which each self-consistent iteration is composed of two steps.

In the first, the 'linear MTO' basis is formed using v_0.[50–53,72] Linear MTO bases are created by fixing the energy E in Eq. 28 and supplementing the basis with the energy derivative of Eq. 28,

$$H_r[v_0]\dot{g}_\kappa(r) = g_\kappa(r) + E\dot{g}_\kappa(r). \tag{29}$$

Here, $\dot{g}_\kappa(r)$ is the energy derivative of g_κ. The solutions g_κ and $\dot{g}_\kappa$ within this spherically symmetric potential at a fixed energy E provide a linear approximation to the basis around energy E. Note that the radial Hamiltonians are only used within the muffin tin spheres to form the basis. For the core states, this is all that is needed since the states do not extend spatially beyond the muffin tins. The valence states in the interstitial are matched to the radial states in the muffin tins and are used to construct Bloch wavefunctions that obey the translational symmetry of the crystal.

In the second step, the density and full potential (Eq. 15) are formed using the linear MTO basis. The core states contribute to the density, while the valence states in both the muffin tins and interstitial region are

used to form the Hamiltonian. The Hamiltonian is then diagonalized and a new density and potential are formed. The next self-consistent iteration can then proceed, using the updated density, potential, and energy eigenvalues. The new potential and eigenvalues are used to generate both a new set of core states and a new set of valence states. Additional details on these steps can be found in ref. 50.

The `dirac-fp` and RSPt codes allow for a variety of ways to treat the basis of the valence states. We focus here on two important choices of the basis with two different treatment of the radii: double and full bases combined with FF and FR approaches. The distinction between double basis and full basis calculations has to do with the number of "tails" used to treat the s and p states in the interstitial region.[52,53] The tails are the solutions outside of the muffin tins (as opposed to the "heads" which are solutions inside the muffin tins). Generally the tails can be expanded in a basis consisting of different numbers of elements. Here, we focus on two choices: a double basis that uses two tails for each s and p state, and a full basis that uses 3 tails for each. Note that d and higher states always use 2 tails. We refer to the case of three tails for the s and p states as a full basis, rather than triple basis, because adding more tails often leads to an overdetermined system and therefore does not increase the accuracy of the calculation. Below, we present a comparison of double and full basis calculations on thorium and find that the full basis provides more consistent results (see Sec. III A).

The distinction between FR and FF has to do with how the muffin tin radii are set. FR methods use the same radius for the muffin tin radii across a series of different computational cell volumes, for example in computing energy-volume (E-V) curves, as done in Sec. III. Importantly, this means that the radius must be small enough to ensure that no two muffin tin spheres overlap in the smallest volume case, thus setting an upper-bound on the muffin tin radius. The FF case instead fixes the fraction of the volume of the computational cell that is allotted to each atom in the cell by specification of the FF radius $S \leq 1$, defined as the ratio of the muffin tin radius to the radius corresponding to the volume of the unit cell. More precisely, for a unit cell with volume V_{cell} that holds a single atom, we define a radius R such that $V_{\text{cell}} = \frac{4}{3}\pi R^3$. The FF ratio is then defined as $S = R_{\text{mt}}/R$, where R_{mt} is the muffin tin radius for that atom. The case of multiple atom types in the cell requires generalization, but is unimportant for the results of this paper which deal exclusively with single-element FCC materials.

C. Exchange-Correlation Functionals

All DFT methods must use an expression for the exchange-correlation functional of the density. In formulating the Dirac approach in Sec. II A as we have, we are able to make use of exchange-correlation functionals of the density by neglecting the current density (exploring the effect of the current density will be the focus of a future paper). This allows us to make use of exchange-correlation potentials designed over the past 20-30 years in our approach. Using these functionals allows us to compare the SR, SR+SO, and Dirac methods on an equal footing. In Sec. III we focus on the use of three different exchange-correlation functionals: the local density approximation (LDA) of Perdew and Wang[63] (PW), the generalized gradient approximation of Perdew, Burke, and Ernzerhof[64] (PBE), and the subsystem functional of Armiento and Mattsson[65] (AM05). These three functionals differ in their philosophy and construction, but none of them have been designed specifically to account for systems in which confinement plays a strong role. As an LDA, the PW functional takes into account only the density local to each point, while PBE takes into account the density and the spatial gradient of the density at each point. The AM05 functional is a sub-system functional using the local density and local gradients of the density, and is designed to account for surface effects, which are not taken into account explicitly in PW or PBE.

Fundamentally, new functionals are needed to adequately describe systems in which confinement plays a strong role. Therefore, none of these functionals should be regarded as correctly describing the physics involved in each system. We focus primarily on the results of PBE in Sec. III because it is the most widely used and allows us to compare in a straight-forward way the differences between the three different relativistic treatments: SR, SR+SO, and Dirac. However, we include for each material (Th, Al, and Au) a table summarizing the results of the PW, PBE, and AM05 functionals to show the extent to which the equilibrium volumes and bulk moduli differ among these three different functionals. Notably, these functionals give quite different results in the case of thorium and to a lesser extent in gold, which provides evidence for the fundamental need for functionals that describe localization.

III. RESULTS

A. Thorium

To investigate the SR, SR+SO, and Dirac treatments, we begin with thorium ($Z = 90$) in its FCC phase. The electron configuration for thorium is [Rn]$6d^2 7s^2$. For all methods (SR, SR+SO, and Dirac), we treat the valence in the same way, using the states $6s6p7s7p6d5f$, with the rest of the lower energy states treated in the core. Among states below the $6s$ manifold, the $5d$ are closest in energy, lying 41 eV below the $6s$ states. This indicates that all states below the $6s$ can be safely treated in the core; the rest must be treated in the valence to allow for the possibility of hybridization. In principle, it is possible that $5g$ states may need to be included in the valence, however

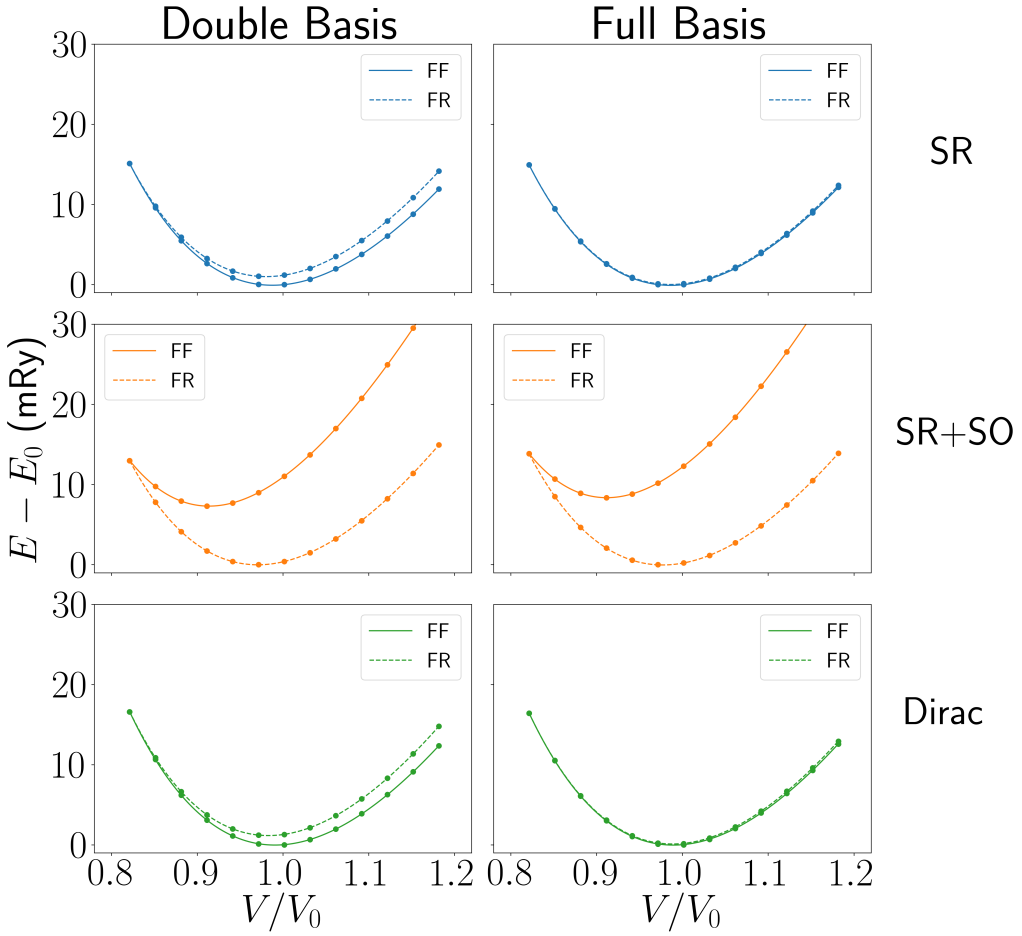

FIG. 2. Energy-volume curves for thorium using the SR (first row), SR+SO (second row), and Dirac (third row) methods and the PBE exchange-correlation functional. The first column shows results using a double basis and the second column shows results using a full basis. In each subplot, the fixed volume fraction (FF) curve is shown as a solid line and the fixed radius (FR) curve is shown as a dashed line. The zero of energy E_0 is different for each subplot, and is taken to be the minimum energy among both curves in the subplot, so that the curves can be compared in a more straight-forward manner. The experimental value of $V_0 = 220.0$ Bohr^3 (ref. 73) is used to normalize the x-axis. The bulk modulus for thorium is 54 GPa (ref. 74).

we find that the results do not change appreciably when these states are left out (see Supplemental Material[75] Sec. 5 for details).

We first explore the effect of using double and full bases for thorium, as well as the use of the FF and FR methods, to compute energy-volume (E-V) curves. In Fig. 2, we plot the E-V curves for double basis (first column) and full basis (second column) for each of the three methods: SR (first row), SR+SO (second row), and Dirac (third row). In each subplot of Fig. 2, the FF curves are shown in solid lines, while the FR curves are shown in dashed lines. For each subplot the zero of energy is chosen to be the lowest energy value computed for both curves in that subplot (i.e., E_0 is different for each subplot). The value V_0 on the x-axis is the experimental equilibrium volume for thorium,[73] $V_0 = 220.0$ Bohr^3 (note that this value includes a zero-point anharmonic expansion correction). Comparisons to other DFT-calculated values are provided in Supplemental Material[75] Sec. 6.

The FF curves shown in Fig. 2 are each computed using FF ratio $S = 0.85$, which is found to give minimal error in equilibrium volume (Supplemental Material[75] Sec. 1 for details). In addition, we use for all calculations a $16\times16\times16$ k-point mesh, which corresponds to 85 points in the irreducible part of the Brillouin zone. This mesh size gives equilibrium volumes accurate to approximately 0.1% of a reference solution computed with a $32\times32\times32$ k-point mesh (489 total points) and can therefore be regarded as converged (see Supplemental Material[75] Sec. 2 for details). The Brillouin zone integration is carried out using tetrahedral integration with the Fermi surface correction of Blöchl.[76] After computing a series of E-V values, we use a Murnaghan[77] fit (described in Supplemental Material[75] Sec. 3) to interpolate between values and compute V_0. We also use the PBE[64] exchange-correlation functional for all figures below.

In each of the double basis calculations, the FF and FR curves do not coincide except at the point corresponding

	V_0 (Bohr^3)			B (GPa)		
	AM05	**PBE**	**PW**	**AM05**	**PBE**	**PW**
SR	204.2	217.0	199.4	58.7	54.9	65.1
SR+SO (FF)	188.9	200.6	185.9	75.5	69.1	83.2
SR+SO (FR)	201.4	214.9	197.9	62.1	57.2	67.7
Dirac	205.5	217.6	201.0	62.2	58.2	67.8

TABLE I. Calculated equilibrium volumes and equilibrium bulk moduli of thorium for SR, SR+SO, and Dirac using three different exchange-correlation functionals: PW, PBE, and AM05. The experimental values of V_0 and B for thorium are 220.0 Bohr^3 (ref. 73) and 54 GPa (ref. 74), respectively.

to the lowest volume, which are chosen to have the same muffin tin radius. On the other hand, the full basis calculations for SR and Dirac lie closely on top of each other, indicating that the choice of FF or FR does not lead to any significant difference in results. This finding can be attributed to the full basis providing a more complete representation of the wavefunctions in the interstitial region.

Unlike for the SR and Dirac methods, however, the SR+SO full basis calculations show a large deviation in E-V curves when using FF and FR. This shows that the part of the total energy arising from the spin-orbit term has a strong dependence on the muffin tin volume. In this case, the SR+SO results give very different equilibrium volumes (roughly 10%) depending on whether FF or FR is used. In the FR SR+SO case, the predicted V_0 values are much closer to the SR and Dirac values (see Table I). This is because in the FR case, the SO term is calculated using the same muffin tin volume for each unit cell. In this case, the part of the total energy arising from the SO term does not change much across different unit cell volumes, whereas a large difference is seen in the FF case. Note that this will not always be the case, as seen for the FR SR+SO results in gold in Sec. III C. In addition, although we see agreement in the E-V curves in thorium for FR SR+SO and the SR and Dirac methods, in the FR SR+SO method a large amount of the SO energy is missing from the calculation, due to the fact that the muffin tin radius must be small enough to fit within the smallest unit-cell volume studied and the SO term is neglected in the interstitial region. Although this does not result in severe differences in the E-V curves in thorium near equilibrium, this could present very important differences under high compression, where SO effects become even more pronounced and it is not physically accurate to throw out large amounts of the SO term. As mentioned previously, some codes implement the SO term throughout the entire unit cell volume,[60,62] which offers obvious advantages. Nevertheless, in muffin tin-based all-electron solid-state codes, the SO term is neglected in the interstitial region, so that this issue should be seen in methods other than FP-LMTO.

We draw two important conclusions from Fig. 2: (1) it is necessary to use a full basis to describe the states treated in the valence when using SR or Dirac and (2) a full basis treatment of the valence states in the SR+SO method does not resolve the large differences in the E-V curves computed using the FF and FR methods, due to the strong energy dependence of the SO term on the muffin tin volume and the neglect of the SO term in the interstitial region. Based on conclusion (1), we use only full basis calculations in the remainder of this paper. In addition, we use only the FF method for SR and Dirac throughout the remainder of this paper, since the FF and FR curves are nearly identical for those methods. For the SR+SO method, we include both the FR and FF results.

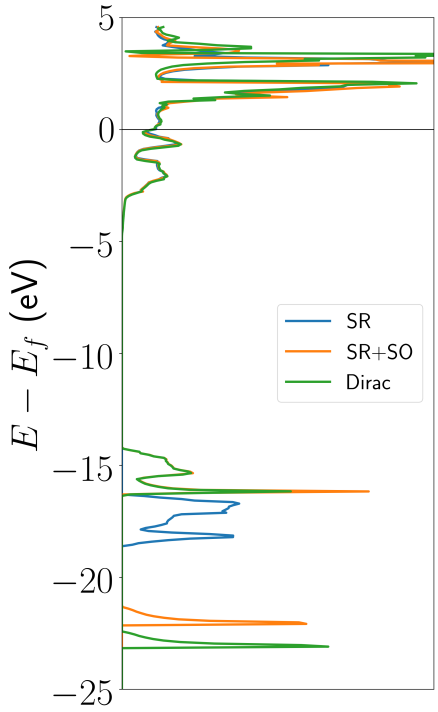

FIG. 3. Electronic density of states of thorium for SR, SR+SO, and Dirac methods. The energy level splitting of the 6p states appear only for the SR+SO and Dirac methods. All results are computed using PBE at the equilibrium volume and FF ratio $S = 0.85$.

To further investigate the adequacy of SR, SR+SO, and Dirac methods for thorium, we compute the electronic density of states for each structure at the experimental equilibrium volume ($V_0 = 220.0$ Bohr^3),[73] shown in Fig. 3. Here we notice that the densities of states near

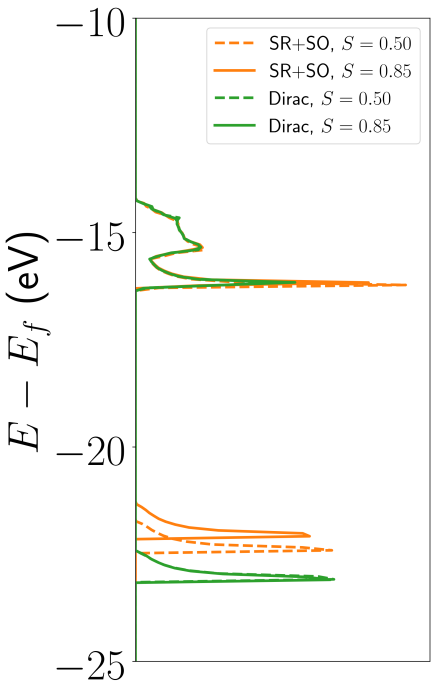

FIG. 4. Electronic density of states for thorium using SR+SO and Dirac, but with different FF radii. The $S = 0.50$ results are shown as dashed lines, while the solid lines use $S = 0.85$. The lower energy SR+SO $6p_{1/2}$ states exhibit a large shift in energy upon changing S, while the Dirac method shows no such shift. All curves use PBE.

the Fermi level E_f are roughly the same for all three methods. However, we notice a large discrepancy for states lying below the Fermi level. Both the SR+SO and Dirac methods predict an energy level splitting of the $6p$ states, while the SR method does not predict a splitting. This splitting corresponds to the $6p_{1/2}$ and $6p_{3/2}$ states found from the solution of the Dirac equation.

Although the SR+SO and Dirac methods both produce the $6p$ energy level splitting, the energy levels are different. The reason for this difference is well-known and is primarily a result of the different $r \to 0$ behavior of the SR $6p$ and Dirac $6p_{1/2}$ states. The SR $6p$ states approach 0 at the origin, as do solutions to the radial Schrödinger equation, whereas the Dirac $6p_{1/2}$ states do not approach 0 and therefore act qualitatively more like s states. These differences are described further in the Supplemental Material[75] Sec. 4. This issue is well known[70,78] and also led developers of the `WIEN97` code (now `WIEN2k`) to provide an "orbital extension" solution to this problem, which adds the Dirac $6p_{1/2}$ states to the SR basis.[54] This fix largely resolves the discrepancy in the energy level splitting between the SR+SO and Dirac methods, as can be seen in ref. 54. Although this addresses the radial behavior of the $6p_{1/2}$ states, the other states remain SR states and therefore the $6p_{1/2}$ correction does not address other differences that result from the use of SR vs. Dirac radial basis functions. In addition, the angular functions used remain SR angular functions, which are different from Dirac angular functions, as seen in Eqs. 18–19, also described in detail in Ch. 2 of ref. 50. These two differences may not result in serious issues near equilibrium, but in compression, it is possible that these differences could become important.

To further explore the electronic structure of thorium, we plot in Fig. 4 the electronic densities of states for SR+SO and Dirac at different radii. We zoom in to states between -25 and -10 eV, as no significant differences are present above -10 eV. In Fig. 4 the green lines correspond to the Dirac treatment and the orange lines correspond to the SR+SO treatment, while solid lines correspond to $S = 0.85$ and dashed lines correspond to $S = 0.50$. In this case, we see a clear shift in the energy of the $6p_{1/2}$ band near -22 eV for the SR+SO method, whereas we see no shift using the Dirac method. This highlights the strong dependence of the SO term on the muffin tin radius in thorium for the $6p$ states. This also raises questions about how to choose the muffin tin radius in the SR+SO method when the implementation neglects the SO term in the interstitial region. In the FR method, multiple choices for the muffin tin radius can be made, and it is not obvious what radius to choose, given the results in Fig. 4. Although it may be possible to partially address this issue with an implementation of the SO term throughout the entire unit cell, this is not typically done in muffin tin methods and doing so would not address other issues, such as the differences in radial and angular basis functions in the SR and Dirac methods. The way we have chosen to address this is to instead switch to the Dirac method, which shows no such dependence on the muffin tin radius, owing to the use of the same Hamiltonian in all parts of the cell.

Before moving on to other materials, we also investigate the role of the exchange-correlation functional on the E-V curves computed. All results in Figs. 2-4 use the PBE[64] exchange-correlation functional, however we also compute the equilibrium volume V_0 and equilibrium bulk modulus B with other functionals, as seen in Table I. We see that the V_0 predicted by PW and AM05 using the SR, SR+SO, and Dirac methods are significantly lower than the V_0 computed for PBE. Although this is the case, none of the functionals are accounting for electron confinement in thorium, so the close prediction of PBE to the experimental value (220.0 Bohr^3)[73] is most likely fortuitous, i.e., due to error cancellation. Importantly, we see a trend within the use of each functional, which is that the FF SR+SO method predicts significantly lower equilibrium volumes than the SR or Dirac methods. This is again attributable to the strong dependence of the SO energy on the muffin tin volume.

The bulk moduli results do not show as obvious a trend. We see that bulk moduli calculated using different exchange-correlation functionals within the SR, FR SR+SO, and Dirac methods deviate up to $\sim$ 10 GPa (18%). The bulk moduli calculated using different exchange-correlation functionals within the FF SR+SO

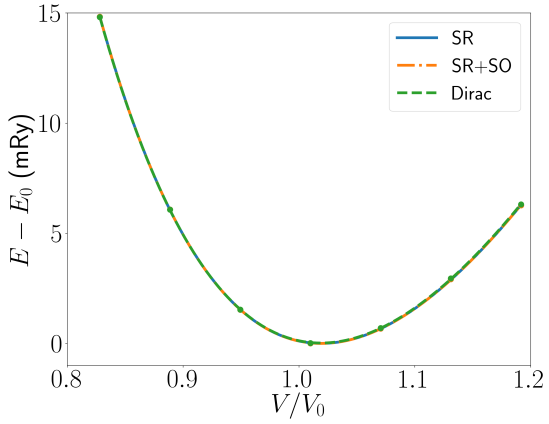

FIG. 5. Energy-volume curves for aluminum for the SR, SR+SO, and Dirac methods. The zero of energy is the same for all curves, so the curves overlap in shape and also in value. For aluminum, $V_0 = 109.5$ Bohr^3.[73]

method deviate up to 14 GPa (20%). However, we also see that the bulk moduli predicted by FF SR+SO are up to 30% higher than those predicted by SR, FR SR+SO, and Dirac within each exchange-correlation functional. This is due to the larger curvature predicted using FF SR+SO that results from including a different SO integration volume for each unit-cell volume. The FR SR+SO values are in much closer agreement with SR and Dirac than FF SR+SO for the same reasons as described above regarding the equilibrium volume predictions.

B. Aluminum

After having looked at the significance of the SR, SR+SO, and Dirac treatments for the heavy element thorium, we now turn our attention to aluminum ($Z = 13$), a material in which relativity should not play a strong role. Aluminum is an FCC material that has an electron configuration [Ne]$3s^2 3p^1$, and we therefore treat the $3s3p$ states in the valence in our calculations.

In Fig. 5, we plot E-V curves for aluminum using SR, SR+SO, and Dirac methods. We use PBE as the exchange-correlation functional, a $16 \times 16 \times 16$ k-point mesh with tetrahedral integration and Blöchl's correction, and FF ratio $S = 0.85$. In all three curves of Fig. 5, the zero of energy is exactly the same.

From Fig. 5, we see that regardless of the method, we get almost exactly the same values along the E-V curve, indicating that relativity does not play an important role and that in this limit, all methods give the same result. This provides validation of the newly-developed Dirac method in cases where relativistic effects are small.

We also show in Table II the values of V_0 and B computed using the AM05, PBE, and PW functionals. In each case, the SR, SR+SO, and Dirac methods give the exact same result, so we list the value only once. The experimental values for aluminum are $V_0 = 109.5$ Bohr^3 (ref. 73, computed using a zero-point anharmonic expansion correction) and $B = 73$ GPa (ref. 79). Comparisons to other DFT-calculated values are provided in Supplemental Material[75] Sec. 6.

	V_0 (Bohr^3)	B (GPa)
AM05	108.7	84.1
PBE	111.6	75.7
PW	106.8	81.3

TABLE II. Calculated equilibrium volumes and equilibrium bulk moduli of aluminum for SR, SR+SO, and Dirac using the semi-core+valence treatment and three different exchange-correlation functionals: PW (LDA), PBE (GGA), and AM05. All values for SR, SR+SO, and Dirac are the same to the nearest tenths digit, and this is also the case when comparing the FF vs. FR treatment for SR+SO. The experimental values of V_0 and B for aluminum are 109.5 Bohr^3 (ref. 73) and 73 GPa (ref. 79), respectively.

C. Gold

The results for thorium and aluminum provide insights into the SR, SR+SO, and Dirac methods for two limiting cases, one where relativistic effects are important and one where they are negligible. To study an intermediate case, we look at gold ($Z = 79$). Gold is an FCC material with electron configuration [Xe]$4f^{14}5d^{10}6s^1$. Gold exhibits a separation in energy between the $6s^1 5d^{10}$ valence electrons and $5s^2 4f^{14} 5p^6$ semi-core electrons and therefore provides two options for choosing the valence states: (1) treating the semi-core electrons *and* valence electrons as the valence states, or (2) treating only the valence electrons in the valence. We consider both cases below. Option 1 is of course needed if we wish to extend the results presented here to high levels of compression. Note also that the $4f$ states for gold have energies between the $5s$ and $5p$ states. This makes it important to treat the $4f$ in the valence, even though the $4f$ states are highly localized and do not extend outside the muffin tin spheres.

In Fig. 6, we plot the E-V curves for the SR, SR+SO, and Dirac methods for gold. We use the PBE exchange-correlation functional, a $16 \times 16 \times 16$ k-point mesh with tetrahedral integration and Blöchl's correction, and FF ratio $S = 0.85$.

In each subplot of Fig. 6, we provide curves for both the case where the semi-core and valence electrons are treated in the valence (solid lines) and the case where only the valence electrons are treated in the valence (dashed lines). In each subplot, a unique value of E_0 is used to determine the relative energy difference in the curves. Notably, the SR and SR+SO methods exhibit a large difference in energy between the semi-core+valence and valence-only curves, so that two axes are needed to represent the energy (values on the left correspond to the valence-only case; values on the right correspond to

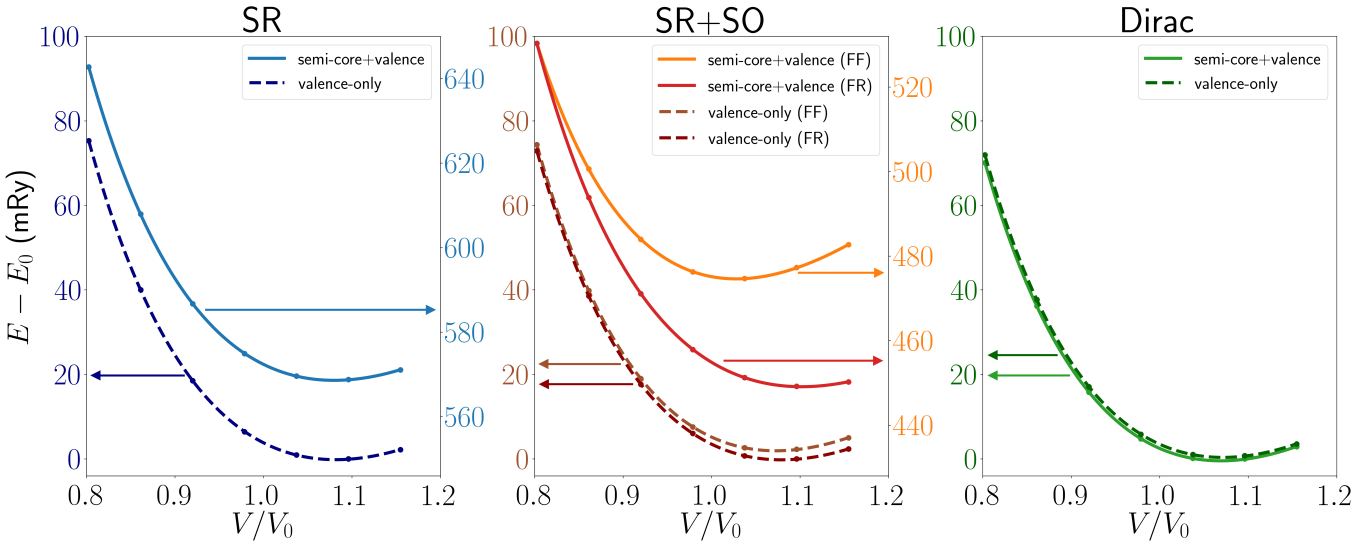

FIG. 6. Energy-volume curves for gold using the SR, SR+SO, and Dirac methods with different choices for which states are chosen as valence states. In each subplot, the solid line shows the case where the $5s^2 4f^{14} 5p^6$ semi-core *and* valence electrons are treated in the valence, while the darker dashed line shows the case where the $5s^2 4f^{14} 5p^6$ semi-core electrons are treated in the core and only the valence electrons are treated as valence states. Each subplot has a unique value of E_0. For the SR and SR+SO methods, the semi-core+valence treatment is significantly higher in energy than the valence-only results, requiring the values to be plotted on two separate y-axes (valence-only values on the left, semi-core+valence values on the right). Arrows point from each curve to the appropriate axis. In the Dirac case, the same y-axis is used for both curves, since the energy values are nearly identical. The range of all y-axes are the same (104 mRy). Notably, the predicted V_0 for valence-only vs. semi-core+valence are the same for the SR and Dirac methods, while the SR+SO method predicts very different values of V_0, depending on which states are treated in the valence. All curves are computed using PBE and FF ratio $S = 0.85$. For gold, $V_0 = 113.0$ Bohr^3 (ref. 73, computed with a zero-point anharmonic expansion correction).

the semi-core+valence case). Unlike the SR and SR+SO methods, the Dirac method gives nearly identical results for the valence-only and semi-core+valence treatments, so that only one y-axis is needed to represent both curves.

We also see from Fig. 6 that the semi-core+valence and valence-only cases individually give very similar values of V_0 in the SR and Dirac methods. The semi-core+valence values of V_0 and B predicted by SR and Dirac differ by less than 1% and less than 4%, respectively. On the other hand, the SR+SO methods gives quite different values for the semi-core+valence and valence-only cases and for both the FF and FR methods. To explain this, we start by looking at the valence-only case (dashed curves only) for SR+SO. In this case the predicted V_0 for FF and FR differ by less than 1%. This indicates that the SO contribution to the valence-only states outside the muffin tins is quite small, therefore leading to small differences in the E-V curves.

The situation is different for the FF and FR SR+SO semi-core+valence curves (solid lines in Fig. 6). Here, the predicted E-V curves are quite different, indicating that the SO energy of the semi-core states has a strong dependence on the muffin tin volume, similar to what was seen in thorium. In the semi-core+valence case, the FF method results in a V_0 that is 4–5% smaller than the V_0 predicted by the SR and Dirac methods and a B that is 15–20% larger than B predicted by the SR and Dirac methods (see Table III). On the other hand, the FR method in SR+SO over-predicts V_0 by 2–3% and under-predicts B by 8–12%, relative to SR and/or Dirac. This indicates that neither the FR nor FF results for SR+SO match very closely with the predictions of SR or Dirac. Furthermore, these differences can be expected to become even more severe in higher compression, where the SO contribution of those states becomes more important.

In Table III we provide V_0 and B values for the SR, SR+SO, and Dirac methods using different exchange-correlation functionals. It is important to point out that PBE tends to overpredict V_0, whereas PW slightly underpredicts V_0 and AM05 is in good agreement with the experimental value $V_0 = 113$ Bohr^3 (computed using a zero-point anharmonic expansion correction, as in ref. 73). Bulk moduli values in Table III can be compared to the experimental value of $B = 167$ GPa (ref. 79). Importantly, within each functional the same trends are seen within the SR, SR+SO (FF and FR), and Dirac methods. Similar to thorium, the SR and Dirac methods predict similar V_0 and B, while the results of the SR+SO method depends critically upon the choice of FF or FR.

Another point regarding the calculations in Fig. 6 is that only the Dirac method is providing very close to the same total energy for the semi-core+valence and valence-only treatments. The reason for this is that in SR and SR+SO, different Hamiltonians are used to treat the va-

	V_0 (Bohr^3)			B (GPa)		
	AM05	**PBE**	**PW**	**AM05**	**PBE**	**PW**
SR	115.0	122.0	112.6	169.6	143.3	188.3
SR+SO (FF)	109.8	116.2	107.9	202.2	170.7	222.1
SR+SO (FR)	116.9	124.5	114.3	159.3	131.6	178.4
Dirac	114.0	120.8	111.7	176.1	149.2	188.3

TABLE III. Calculated equilibrium volumes and equilibrium bulk moduli of gold for SR, SR+SO, and Dirac for the semi-core+valence treatment and using three different exchange-correlation functionals: PW, PBE, and AM05. The experimental values of V_0 and B for gold are 113.0 Bohr^3 (ref. 73) and 167 GPa (ref. 79), respectively.

lence and core states, as shown in Fig. 1. The Dirac method does not suffer from this issue because all states are treated with the Dirac Hamiltonian.

Having analyzed the E-V curves in Fig. 6, we now turn to the electronic density of states of gold. In Fig. 7, we plot the density of states of the $5p$ levels at different volumes using the semi-core+valence treatment. In the figure, V_0 is the experimental value, 113 Bohr^3 (see ref. 73). Here, the $5p$ SR states are shown in blue, while the $5p_{1/2}$ and $5p_{3/2}$ Dirac states are shown in green. The SR+SO $5p$ states, which are split by the SO term are shown in orange solid and brown dashed lines, corresponding to the FF and FR treatments, respectively. Similar to the $6p_{1/2}$ Dirac states in thorium, the $5p_{1/2}$ Dirac states in gold have a different $r \to 0$ behavior than the $5p$ SR states. This leads to a different prediction of the energy level of the $5p_{1/2}$ states for SR+SO and Dirac. In addition to this, we see that as V/V_0 changes, the SR+SO FF and FR methods predict slightly different $5p_{1/2}$ energy levels, due to the use of a different muffin tin volume used to take matrix elements of the SO potential.

In addition to the difference in predicted energy levels of the $5p_{1/2}$ states, we also see differences in the $4f$ energy levels predicted by the SR+SO and Dirac methods, as shown in Supplemental Material[75] Sec. 7. In the $4f$ case, the $4f_{5/2}$ and $4f_{7/2}$ energy levels predicted by the Dirac method are higher in energy than those predicted by the SR+SO method, which is the opposite trend seen for the $5p_{1/2}$ states. These differences will of course become more pronounced under higher levels of compression, where the $4f$ states can broaden and potentially hybridize with other states.

The study of gold allows us to draw several conclusions. First, we see that the valence-only treatment of the states leads to very similar E-V curves in Fig. 6, regardless of choice of method. In this case, states below the $6s$ manifold are all treated with the Dirac equation, so the only differences among treatments occurs in the way that the SO term is applied to the valence states. On the other hand, larger differences in the predicted E-V curves are seen for the semi-core+valence treatment. Similar to the case of thorium, we see that the semi-core+valence SR and Dirac methods predict similar E-V curves near equilibrium, while the SR+SO FF and FR methods predict significantly different V_0 and/or B, as seen in Table III and as described above. The differences in the semi-core+valence SR+SO FF and FR E-V curves are, similar to the case of thorium, due largely to the neglect of the SO term in the interstitial region. However, while the FR SR+SO E-V curves in thorium agreed quite closely with the SR and Dirac E-V curves, we do not see the same level of agreement in the FR SR+SO and SR or Dirac E-V curves in gold. This indicates that the use of the FR SR+SO method will not always be adequate for predicting equilibrium properties when a semi-core+valence treatment is required.

In addition, we see significant differences in the electronic structure of gold predicted by SR, SR+SO, and Dirac. Similar to the thorium $6p_{1/2}$ states, the gold $5p_{1/2}$ SR and Dirac states have different $r \to 0$ behavior and therefore lead to a difference in the predicted energy levels of these states. We also see differences in the predicted energy levels of the $4f_{5/2}$ and $4f_{7/2}$ states between SR+SO and Dirac, as shown in Supplemental Material[75] Sec. 7. Although the $4f$ and $5p$ states are well-localized near equilibrium, under higher levels of compression, they can start to broaden and hybridize. When this occurs, the differences in the electronic structures seen in Fig. 7 and in Supp. Material Sec. 7 will become increasingly important and are likely to lead to different predictions in the E-V curves at small volumes.

IV. CONCLUSION

We have developed a new methodology for computing the properties of materials based on the Dirac-Kohn-Sham equations. The code we have developed, `dirac-fp`, is based on the FP-LMTO code RSPt, but solves the Dirac equation throughout all parts of the computational cell. We use the Dirac method and the SR and SR+SO methods in RSPt to assess the performance of different relativistic treatments on an equal footing.

For thorium, we find that the use of a double basis leads to inconsistent results when treating the muffin tin radii with the FR and FF choices in both the SR and Dirac methods. This issue is resolved in the case of the SR and Dirac methods when using a full basis, which provides a more complete representation of the wavefunctions in the interstitial region. For the SR+SO method, however, the resulting E-V curves using FR and FF are very different and the discrepancies do not go away when

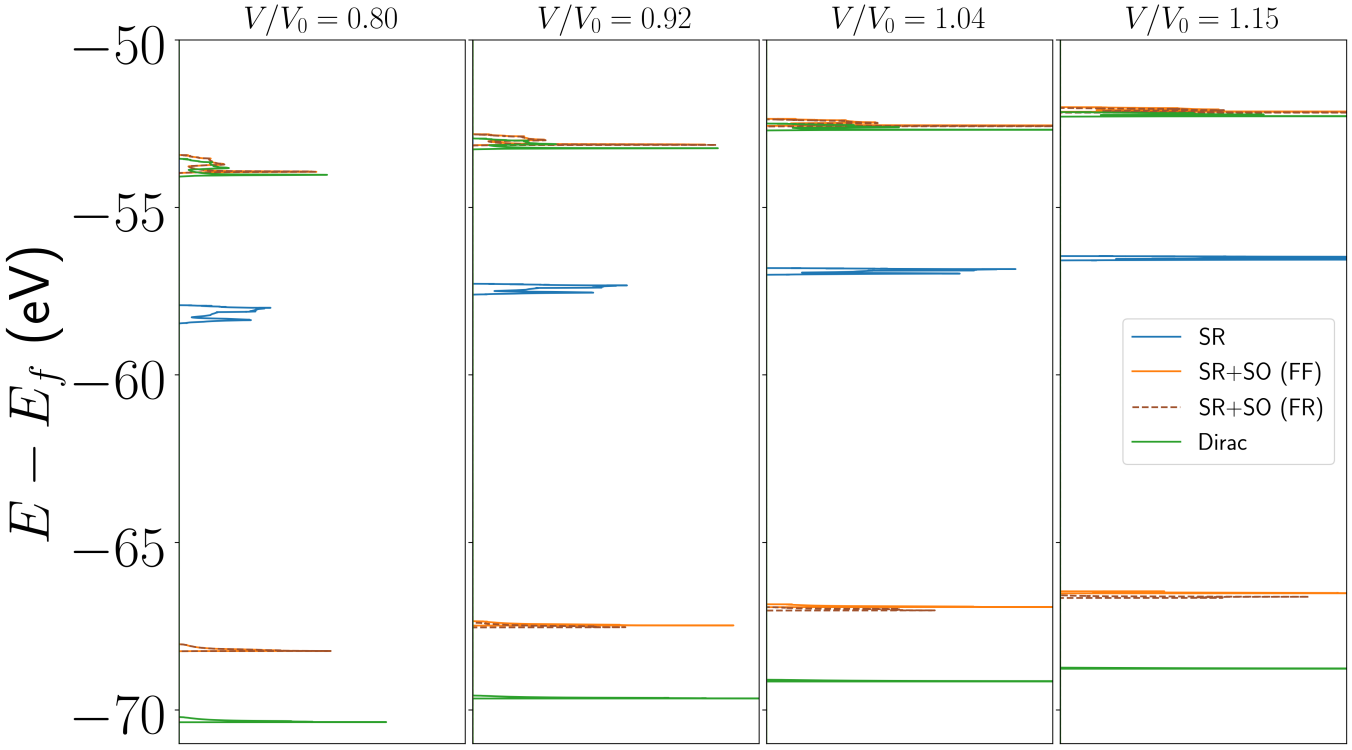

FIG. 7. Electronic densities of $5p$ states for gold at different unit-cell volumes using the semi-core+valence treatment and the PBE exchange-correlation functional. SR and Dirac FF curves are shown in blue and green, respectively, while the SR+SO method shows curves for the FF (orange lines) and FR (brown dashed lines) treatments. The muffin tin radii at $V/V_0 = 0.8$ are the same for the FR and FF methods, leading identical densities of states. The SR $5p$ states are split into a $5p_{1/2}$ (below -65 eV) and $5p_{3/2}$ (above -55 eV) when adding the SO term, though the SR+SO $5p_{1/2}$ states do not match the Dirac $5p_{1/2}$ states in energy, owing primarily to the different $r \to 0$ behavior of the SR and Dirac $5p_{1/2}$ radial functions. For gold, $V_0 = 113.0$ Bohr^3 (ref. 73, computed with a zero-point anharmonic expansion correction).

switching from a double to full basis. The difference in SR+SO FF and FR E-V curves in thorium is a result of the strong dependence of the SO energy on the muffin tin volume and the neglect of the SO term in the interstitial. In the FR case, the contribution of the SO term to the total energy is roughly the same across the different unit cell volumes, so that the predicted V_0 and B do not differ significantly from V_0 and B predicted by SR and Dirac. On the other hand, in the FF method, the SO contribution to the total energy changes as the unit-cell and muffin tin volumes change, leading to E-V curves that differ significantly from the SR and Dirac E-V curves. Although these issues could potentially be addressed by incorporating the SO term in the interstitial region, it is not obvious how to do so within muffin tin-based methods, and therefore this issue will be relevant for other codes using similar treatments of the SO term. These issues are all addressed in the Dirac method.

We also see in thorium that the electronic structures computed using SR, SR+SO, and Dirac are very different. In particular, we see the well-known splitting of the $6p$ SR states into $6p_{1/2}$ and $6p_{3/2}$ levels in the SR+SO and Dirac methods. Although the $6p$ splitting is present in SR+SO, the $6p_{1/2}$ levels are not the same as the $6p_{1/2}$ Dirac states primarily because of the different $r \to 0$ behavior of the $6p$ SR and $6p_{1/2}$ Dirac states. We also find that the SR+SO $6p_{1/2}$ energy levels depend strongly on the muffin tin radius, due to the neglect of the SO term in the interstitial. In the Dirac implementation, the correct radial behavior of the $6p_{1/2}$ states is implicit. Furthermore, other differences between the SR and Dirac radial and angular states are included in the Dirac implementation, which could become increasingly important when studying high compression.

We find in the case of the light element aluminum that the SR, SR+SO, and Dirac treatments all produce nearly identical results. This serves as a validation of `dirac-fp` in the non-relativistic limit. Furthermore, we find that all three methods give nearly identical results for V_0 and B across different exchange-correlation functionals.

For gold, we find that the Dirac treatment produces nearly identical results when treating the $5s^2 4f^{14} 5p^6$ semi-core electrons in the core or as part of the valence. The SR method predicts roughly the same V_0 and B for both treatments of the semi-core states, so that the two treatments do not lead to significantly different predictions of equilibrium properties.

In the SR+SO method, we see that the valence-only

FF and FR treatments lead to similar E-V curves that do not differ significantly from the SR and Dirac results, whereas the semi-core+valence FF and FR treatments lead to E-V curves that differ substantially from the SR or Dirac semi-core+valence curves. In particular, the FF and FR SR+SO methods predict a B that is too high and too low, respectively. Similarly to thorium, these issues arise primarily from the neglect of the SO term in the interstitial region. This highlights the need to use caution when interpreting results from the SR+SO method as more states are added to the valence.

In addition to this, we see differences in the electronic structure of the $5p$ and $4f$ states in gold. The issue of the incorrect $5p_{1/2}$ levels predicted by SR+SO is qualitatively similar to the $6p_{1/2}$ issue seen in thorium. However, we also see that the $4f_{5/2}$ and $4f_{7/2}$ levels differ between SR+SO and Dirac. These issues again highlight the need to use caution when using similar treatments of the SO term, particularly when including semi-core states in the valence.

The findings of the present strudy present strong evidence for the usefulness of the Dirac method when studying solids containing heavy elements. The Dirac method allows for the correct radial and angular functions to be included in the calculation from the start and also provides a foundation for building in additional terms in the Dirac-Kohn-Sham equations. In particular, the effective vector potential terms that depend on the current density can be added in order to provide a more complete description of relativistic effects in materials. We have shown that the SR and SR+SO methods cannot simultaneously predict the equilibrium properties and electronic structure found when using the Dirac method. These differences are likely to become increasingly important under higher compression, where we expect the Dirac method to be most useful.

ACKNOWLEDGEMENTS

This work was supported in part by Advanced Simulation and Computing, Physics and Engineering Models, at Los Alamos National Laboratory. Los Alamos National Laboratory, an affirmative action/equal opportunity employer, is managed by Triad National Security, LLC, for the National Nuclear Security Administration of the U.S. Department of Energy under contract 89233218CNA000001.

This work was also supported in part by the Laboratory Directed Research and Development Program at Sandia National Laboratories. We also acknowledge support from the Nuclear Energy Advanced Modeling and Simulation (NEAMS) programs Fundamental Methods and Models element. Sandia National Laboratories is a multimission laboratory managed and operated by National Technology & Engineering Solutions of Sandia, LLC, a wholly owned subsidiary of Honeywell International Inc., for the U.S. Department of Energys National Nuclear Security Administration under contract DE-NA0003525.

[1] P. Hohenberg and W. Kohn, Physical Review **136**, B864 (1964).
[2] W. Kohn and L. J. Sham, Physical Review **140**, A1133 (1965).
[3] J. P. Perdew and K. Schmidt, in *AIP Conference Proceedings*, Vol. 577 (AIP, 2001) pp. 1–20.
[4] A. E. Mattsson, Science **298**, 759 (2002).
[5] B. Johansson, Philosophical Magazine **30**, 469 (1974).
[6] J. Allen and R. M. Martin, Physical Review Letters **49**, 1106 (1982).
[7] M. Lavagna, C. Lacroix, and M. Cyrot, Physics Letters A **90**, 210 (1982).
[8] B. Johansson, I. Abrikosov, M. Aldén, A. Ruban, and H. L. Skriver, Physical Review Letters **74**, 2335 (1995).
[9] J. Allen and L. Liu, Physical Review B **46**, 5047 (1992).
[10] P. Söderlind, EPL (Europhysics Letters) **55**, 525 (2001).
[11] P. Söderlind and B. Sadigh, Physical Review Letters **92**, 185702 (2004).
[12] P. Sderlind, A. Landa, and B. Sadigh, Advances in Physics **68**, 1 (2019).
[13] P. Söderlind, O. Eriksson, B. Johansson, and J. Wills, Physical Review B **50**, 7291 (1994).
[14] J. M. Wills and O. Eriksson, Los Alamos Science **26**, 128 (2000).
[15] F. Hao, R. Armiento, and A. E. Mattsson, Physical Review B **82**, 115103 (2010).
[16] F. Hao, R. Armiento, and A. E. Mattsson, The Journal of chemical physics **140**, 18A536 (2014).
[17] A. Rajagopal and J. Callaway, Physical Review B **7**, 1912 (1973).
[18] A. Rajagopal, Journal of Physics C: Solid State Physics **11**, L943 (1978).
[19] A. H. MacDonald and S. Vosko, Journal of Physics C: Solid State Physics **12**, 2977 (1979).
[20] R. M. Dreizler and E. K. Gross, *Density functional theory: an approach to the quantum many-body problem* (Springer Science & Business Media, 2012).
[21] R. Dreizler, "Relativistic density functional theory," in *A Primer in Density Functional Theory*, edited by C. Fiolhais, F. Nogueira, and M. A. L. Marques (Springer Berlin Heidelberg, Berlin, Heidelberg, 2003) pp. 123–143.
[22] E. Engel, in *Theoretical and Computational Chemistry*, Vol. 11 (Elsevier, 2002) pp. 523–621.
[23] E. Engel and R. Dreizler, in *Density Functional Theory II* (Springer, 1996) pp. 1–80.
[24] E. Engel and R. M. Dreizler, *Density functional theory* (Springer, 2013).
[25] K. Koepernik and H. Eschrig, Physical Review B **59**, 1743 (1999).
[26] H. Eschrig, M. Richter, and I. Opahle, in *Theoretical*

and Computational Chemistry, Vol. 14 (Elsevier, 2004) pp. 723–776.
[27] M. Kadek, M. Repisky, and K. Ruud, Physical Review B **99**, 205103 (2019).
[28] W. Liu, F. Wang, and L. Li, Journal of Theoretical and Computational Chemistry **2**, 257 (2003).
[29] R. Zhao, Y. Zhang, Y. Xiao, and W. Liu, The Journal of chemical physics **144**, 044105 (2016).
[30] K. G. Dyall and K. Fægri Jr, *Introduction to relativistic quantum chemistry* (Oxford University Press, 2007).
[31] M. Pepper and B. E. Bursten, Chemical Reviews **91**, 719 (1991).
[32] P. Pyykko, Chemical Reviews **88**, 563 (1988).
[33] DIRAC, a relativistic ab initio electronic structure program, Release DIRAC18 (2018), written by T. Saue, L. Visscher, H. J. Aa. Jensen, and R. Bast, with contributions from V. Bakken, K. G. Dyall, S. Dubillard, U. Ekström, E. Eliav, T. Enevoldsen, E. Faßhauer, T. Fleig, O. Fossgaard, A. S. P. Gomes, E. D. Hedegård, T. Helgaker, J. Henriksson, M. Iliaš, Ch. R. Jacob, S. Knecht, S. Komorovský, O. Kullie, J. K. Lærdahl, C. V. Larsen, Y. S. Lee, H. S. Nataraj, M. K. Nayak, P. Norman, G. Olejniczak, J. Olsen, J. M. H. Olsen, Y. C. Park, J. K. Pedersen, M. Pernpointner, R. di Remigio, K. Ruud, P. Sałek, B. Schimmelpfennig, A. Shee, J. Sikkema, A. J. Thorvaldsen, J. Thyssen, J. van Stralen, S. Villaume, O. Visser, T. Winther, and S. Yamamoto (available at https://doi.org/10.5281/zenodo.2253986, see also http://www.diracprogram.org).
[34] S. Fritzsche, C. F. Fischer, and G. Gaigalas, Computer physics communications **148**, 103 (2002).
[35] C. F. Fischer, G. Tachiev, G. Gaigalas, and M. R. Godefroid, Computer physics communications **176**, 559 (2007).
[36] L. Visscher, O. Visser, P. J. Aerts, H. Merenga, and W. Nieuwpoort, Computer physics communications **81**, 120 (1994).
[37] L. Belpassi, F. Tarantelli, A. Sgamellotti, and H. M. Quiney, Physical Review B **77**, 233403 (2008).
[38] L. Belpassi, L. Storchi, H. M. Quiney, and F. Tarantelli, Physical Chemistry Chemical Physics **13**, 12368 (2011).
[39] T. Shiozaki, Wiley Interdisciplinary Reviews: Computational Molecular Science **8**, e1331 (2018).
[40] H. Quiney and P. Belanzoni, The Journal of chemical physics **117**, 5550 (2002).
[41] A. Willetts, L. Gagliardi, A. G. Ioannou, C.-K. Skylaris, S. Spencer, N. C. Handy, and A. M. Simper, International Reviews in Physical Chemistry **19**, 327 (2000).
[42] J. Hubbard, Proceedings of the Royal Society of London. Series A. Mathematical and Physical Sciences **276**, 238 (1963).
[43] V. I. Anisimov, F. Aryasetiawan, and A. Lichtenstein, Journal of Physics: Condensed Matter **9**, 767 (1997).
[44] B. Himmetoglu, A. Floris, S. De Gironcoli, and M. Cococcioni, International Journal of Quantum Chemistry **114**, 14 (2014).
[45] V. Anisimov and O. Gunnarsson, Physical Review B **43**, 7570 (1991).
[46] V. Anisimov, A. Poteryaev, M. Korotin, A. Anokhin, and G. Kotliar, Journal of Physics: Condensed Matter **9**, 7359 (1997).
[47] G. Kotliar, S. Y. Savrasov, K. Haule, V. S. Oudovenko, O. Parcollet, and C. Marianetti, Reviews of Modern Physics **78**, 865 (2006).
[48] F. Aryasetiawan and O. Gunnarsson, Reports on Progress in Physics **61**, 237 (1998).
[49] X. Ren, P. Rinke, C. Joas, and M. Scheffler, Journal of Materials Science **47**, 7447 (2012).
[50] D. A. Rehn, T. Björkman, A. E. Mattsson, and J. M. Wills, *Relativistic density functional theory in the full potential linear muffin tin orbital method*, Tech. Rep. (2019) LA-UR-19-32606.
[51] J. M. Wills, O. Eriksson, M. Alouani, and D. L. Price, in *Electronic Structure and Physical Properies of Solids* (Springer, 1999) pp. 148–167.
[52] J. M. Wills, M. Alouani, P. Andersson, A. Delin, O. Eriksson, and O. Grechnyev, *Full-Potential Electronic Structure Method: energy and force calculations with density functional and dynamical mean field theory*, Vol. 167 (Springer Science & Business Media, 2010).
[53] T. Bjrkman, *Magnetic and Structural Properties of f-electron Systems from First Principles Theory*, Ph.D. thesis (2009).
[54] J. Kuneš, P. Novak, R. Schmid, P. Blaha, and K. Schwarz, Physical Review B **64**, 153102 (2001).
[55] J. J. Sakurai, *Advanced quantum mechanics* (Pearson Education India, 1967).
[56] B. Zimmermann, M. Heide, G. Bihlmayer, and S. Blügel, Physical Review B **90**, 115427 (2014).
[57] P. Novak, Calculation of spin-orbit coupling. Notes incporporated with the Wien2k code, http://susi.theochem.tuwien.ac.at/reg_user/textbooks/novak_lecture_on_spinorbit.pdf.
[58] A. MacDonald, W. Picket, and D. Koelling, Journal of Physics C: Solid State Physics **13**, 2675 (1980).
[59] A. Gulans, S. Kontur, C. Meisenbichler, D. Nabok, P. Pavone, S. Rigamonti, S. Sagmeister, U. Werner, and C. Draxl, Journal of Physics: Condensed Matter **26**, 363202 (2014).
[60] E. v. Van Lenthe, J. Snijders, and E. Baerends, The Journal of chemical physics **105**, 6505 (1996).
[61] V. Blum, R. Gehrke, F. Hanke, P. Havu, V. Havu, X. Ren, K. Reuter, and M. Scheffler, Computer Physics Communications **180**, 2175 (2009).
[62] W. P. Huhn and V. Blum, Physical Review Materials **1**, 033803 (2017).
[63] J. P. Perdew and Y. Wang, Physical Review B **45**, 13244 (1992).
[64] J. P. Perdew, K. Burke, and M. Ernzerhof, Physical Review Letters **77**, 3865 (1996).
[65] R. Armiento and A. E. Mattsson, Physical Review B **72**, 085108 (2005).
[66] W. Gordon, Zeitschrift für Physik **50**, 630 (1928).
[67] D. Koelling and B. Harmon, Journal of Physics C: Solid State Physics **10**, 3107 (1977).
[68] J. K. e. a. Dewhurst, "The elk code," http://elk.sourceforge.net.
[69] P. Blaha, K. Schwarz, G. K. Madsen, D. Kvasnicka, and J. Luitz, An augmented plane wave+ local orbitals program for calculating crystal properties (2001).
[70] L. Nordström, J. Wills, P. H. Andersson, P. Söderlind, and O. Eriksson, Physical Review B **63**, 035103 (2000).
[71] K. Lejaeghere, G. Bihlmayer, T. Björkman, P. Blaha, S. Blügel, V. Blum, D. Caliste, I. E. Castelli, S. J. Clark, A. Dal Corso, *et al.*, Science **351**, aad3000 (2016).
[72] O. K. Andersen, Physical Review B **12**, 3060 (1975).
[73] P. Haas, F. Tran, and P. Blaha, Physical Review B **79**, 085104 (2009).
[74] C. Kittel, P. McEuen, and P. McEuen, *Introduction to*

solid state physics, Vol. 8 (Wiley New York, 1976).
[75] See Supplemental Material at [URL will be inserted by publisher] for additional information and calculations.
[76] P. E. Blöchl, O. Jepsen, and O. K. Andersen, Physical Review B **49**, 16223 (1994).
[77] F. Murnaghan, Proceedings of the National Academy of Sciences of the United States of America **30**, 244 (1944).
[78] R. Devanathan, L. Van Brutzel, A. Chartier, C. Guéneau, A. E. Mattsson, V. Tikare, T. Bartel, T. Besmann, M. Stan, and P. Van Uffelen, Energy & Environmental Science **3**, 1406 (2010).
[79] A. Dewaele, P. Loubeyre, and M. Mezouar, Physical Review B **70**, 094112 (2004).